Optimizing topical delivery to the ostiomeatal complex after functional endoscopic sinus surgery using a bidirectional delivery method

International Journal of Pharmaceutics 686 (2025) 126333

Contents lists available at ScienceDirect

International Journal of Pharmaceutics

journal homepage: www.elsevier.com/locate/ijpharm

Optimizing topical delivery to the ostiomeatal complex after functional endoscopic sinus surgery using a bidirectional delivery method

Ruiping Ma [a,b], Siping Sun [c], Yusheng Wang [a], Feilun Yang [a], Zehui Li [a], Botao Wang [a], Jingguo Chen [a], Bin Sun [a], Guoxi Zheng [a], Shaokoon Cheng [d], Ya Zhang [a,*], Jingliang Dong [a,b,e,**]

[a] Department of Otolaryngology Head and Neck Surgery & Shaanxi Provincial Key Laboratory for Precision Diagnosis and Treatment of Otorhinolaryngology, The Second Affiliated Hospital of Xi'an Jiaotong University, Xi'an, Shaanxi, China
[b] Institute for Sustainable Industries & Liveable Cities, Victoria University, PO Box 14428, Melbourne, VIC 8001, Australia
[c] Zhejiang Cuize Pharmatech Co., Ltd, China
[d] School of Engineering, Faculty of Science and Engineering, Macquarie University, NSW 2109, Australia
[e] First Year College, Victoria University, Footscray Park Campus, Footscray, VIC 3011, Australia

ARTICLE INFO

Keywords:
Bidirectional drug delivery
Computational fluid dynamics
Discrete phase model
Functional endoscopic sinus surgery
Particle mass distribution
3D printing

ABSTRACT

Chronic rhinosinusitis with nasal polyps (CRSwNP) remains a therapeutic challenge due to frequent recurrence after surgery, largely stemming from inadequate drug delivery to the posterior nasal mucosa, particularly the ostiomeatal complex (OMC). While aerosol dynamics are known to influence intranasal drug deposition, quantitatively assessing deposition patterns within complex nasal anatomies is difficult. This study employed a bidirectional delivery approach using computational fluid dynamics (CFD) simulations based on patient-specific sinonasal cavity models, incorporating realistic polydisperse particle size distributions. The effects of device nosepiece insertion angle, nosepiece wall thickness, and exhalation flow rate on drug delivery efficiency were systematically analyzed. Simulated results were validated against in vitro experiments using 3D-printed nasal cavity replicas. Findings revealed that lateral adjustment of the nosepiece insertion angle significantly enhanced drug deposition in the OMC region, while variations in wall thickness and exhalation flow rate had comparatively modest effects. Particles $\leq$ 15.5 μm and $\geq$52.5 μm showed greater OMC deposition than mid-sized particles, with exhalation flow rate positively correlated with total OMC mass deposition within the 15–45 L/min range. These results highlight the dominant role of nosepiece insertion orientation in optimizing regional delivery and the nuanced effects of particle size and flow dynamics. This study offers a comprehensive framework for evaluating nasal drug delivery performance based on realistic device parameters and particle behavior, providing actionable insights to guide the design of more effective nasal delivery systems for treating CRSwNP.

1. Introduction

Chronic sinusitis with nasal polyp (CRSwNP) poses a significant clinical challenge due to its high recurrence post-surgery rate, primarily attributed to the challenge of precise drug delivery to the diseased posterior nasal mucosa. Studies indicated that the dynamics of aerosol delivery in the respiratory tract play a crucial role in regulating drug deposition efficiency, yet quantifying deposition distribution across anatomical sites remain a daunting task. Recently, Xi et al. developed a segmented nasal model to visualize deposition patterns and quantify regional doses using normal and bidirectional breathing patterns, although only one particle size (3.2 μm) was considered in the study (Xi et al., 2017; Xi et al., 2018). Differences in anatomical structure and administration mode can affect the efficiency of drug deposition,

Abbreviations: BDS, bi-directional delivery system; CFD, computational fluid dynamics; CRSwNP, chronic sinusitis with nasal polyp; CT, Computed Tomography; DE, deposition efficiency; DPM, discrete phase model; FESS, functional endoscopic sinus surgery; HPLC, High Performance Liquid Chromatography; LoS, line of sight; MT, middle turbinectomy; OMC, ostiomeatal complex; SVR, surface area-to-volume ratio.

* Corresponding author at: Department of Otolaryngology Head and Neck Surgery & Shaanxi Provincial Key Laboratory for Precision Diagnosis and Treatment of Otorhinolaryngology, The Second Affiliated Hospital of Xi'an Jiaotong University, 157 Xiwu Road, Xi'an, Shaanxi 710000, China.
** Corresponding author at: Institute for Sustainable Industries & Liveable Cities, Victoria University, PO Box 14428, Melbourne, VIC 8001, Australia.
E-mail addresses: zhangya@xjtu.edu.cn (Y. Zhang), jingliang.dong@vu.edu.au (J. Dong).

https://doi.org/10.1016/j.ijpharm.2025.126333
Received 3 July 2025; Received in revised form 28 October 2025; Accepted 28 October 2025
Available online 2 November 2025

however, the mechanisms and underlying principles governing the multiscale mechanical factors—spanning the airway, delivery device, and drug particles—following nasal endoscopic surgery remain unclear. Considering that aerosol therapy after functional endoscopic sinus surgery (FESS) is routinely employed to reduce inflammation and prevent polyp recurrence, the present study focuses on post-surgical nasal geometries to ensure strong clinical and therapeutic relevance.

A bi-directional delivery system (BDS) uses the patient's exhaled airflow to create soft palate closure and positive pressure, which carries aerosols from one nostril through the nasopharynx and into the contralateral side. Due to these advantages, it has attracted increasing attention in rhinopathy and nasal-cerebral administration (Cassano et al., 2021; Liu and Wu, 2023). Djupesland et al. compared nasal sprays and BDS to the deposition of the human respiratory airway through in vivo experiments and showed that there was no or very little deposition of drug particles in the lungs through BDS (Djupesland, 2013; Djupesland et al., 2020; Djupesland and Skretting, 2012; Djupesland et al., 2004, 2006). Farnoud et al. investigated the effect of expiration-assisted pulsed airflow conditions on nasal aerosol particle deposition and found that pulsed airflow not only reduced total nasal aerosol deposition from 50.9 % to 34.4 %, but also reduced the inhomogeneity of drug particle deposition on the left and right sides of the nasal cavity (Farnoud et al., 2021). Hosseini et al. also emphasized the importance of using pulsed techniques to enhance bidirectional nasal sinus drug delivery (Hosseini and Golshahi, 2019). Dong et al. compared the delivery efficiency of BDS and an aerosol mask system in the olfactory zone of a healthy adult, and showed that the olfactory deposition after BDS was 2 and 7 times higher for 1 nm and 10 μm particles, respectively (Dong et al., 2018). Djupesland compared the effects of BDS and conventional nasal sprays using radiolabeled powder carriers (Djupesland and Skretting, 2012). However, information on regional particle deposition in both experimental and clinical research is still limited due to available measurement techniques (Corcoran, 2015). In addition, previous studies have only used particle deposition efficiency (based on calculated area and total number of particles inhaled) as a performance metric (Calmet et al., 2019; Dong et al., 2018; Wofford et al., 2015). However, in laboratory exposure practice, particle mass (calculated by particle number, diameter, density, and other physicochemical properties) is widely used as a dosage indicator to determine the appropriate dose for inhalation therapy. In addition, nozzle orientation plays an important role in nasal spray drug delivery performance (Tong et al., 2016). However, previous studies have not considered the deformation of the nasal vestibule that occurs when inserting the nosepiece of a nasal spray bottle or a bidirectional delivery system (BDS) device. This deformation is particularly relevant in the case of BDS devices, whose nosepieces are designed to fit snugly within the nasal vestibule and form a seal at the inlet of the targeted nasal chamber. As a result, all exhaled drug-laden airflow can be directed into that specific side of the nasal cavity, and the close fit and sealing between the nosepiece and the nasal vestibule are critical for achieving effective topical administration.

Therefore, this study performed in vitro experiments and particle size analysis of mometasone furoate through BDS in a laboratory environment by 3D printing segmented sinonasal cavities models. A generic BDS device was scanned using high-dose computed tomography. Unlike clinical CT settings optimized for soft tissue, higher X-ray exposure was required to achieve sufficient resolution for accurate reconstruction of the device geometry. This digital model was then integrated with realistic sinonasal cavities, enabling a systematic investigation of nasal airways fitted with a BDS device for the first time. Then mass distribution of drugs delivered in the sinonasal cavities was also analyzed. We acknowledge that the drug delivery process is influenced by multiple factors at the same time. However, in order to narrow the scope of the study to a manageable level, this study focus on the effects of the nosepiece orientation, wall thickness of device nosepiece, and exhalation flow rate on BDS delivery efficiency. By addressing these objectives, this study may lay the groundwork for innovative strategies to optimize drug delivery and improve treatment outcomes for this challenging condition.

2. Material and Methods

2.1. Three-dimensional models

Prior to initiating the study, ethical approval was obtained from the Medical Ethics Committee and Institutional Review Board of the Second Affiliated Hospital of Xi'an Jiaotong University (batch number: 2020–819). Written informed consent was obtained from all participants involved in this research. DICOM files of the paranasal cavities were obtained from CT scans of five patients with CRSwNP who underwent full FESS between September 2021 and October 2022 at the Second Affiliated Hospital of Xi'an Jiaotong University. Patients with significant nasal septum deviation were excluded from this study. The cohort included three males and two females, with a mean age of 35.8 ± 4.3 years. Table 1 presents the geometric characteristics of all nasal cavity models, including each subject's gender, age, surface area, volume, as well as surface area-to-volume ratio (SVR) for each side of the nasal chambers. Nasal subjects A, B, and D underwent complete resection of the uncinate process, wide opening of the maxillary/ frontal/ sphenoid sinuses, and resection of the ethmoidal sinus, with complete middle turbinectomy (MT) during the operation. Nasal subjects C and E underwent nasal polypectomy and bilateral full- sinuses fenestration. The procedures included moderate resection of the uncinate process, opening of the four pairs sinuses, as well as partial MT during surgery. The three-dimensional airway reconstruction procedure has been detailed in our previous studies (Ma et al., 2024a; Ma et al., 2024b; Siu et al., 2020a) and all five airway subjects are shown in Fig. 1. To simulate the actual use of the bidirectional drug delivery system (BDS), the device's nosepiece was positioned within the nasal vestibule of all nasal subjects (Fig. 2). The schematic diagrams were depicted on a representative nasal airway model (i.e. model A). Compared to previous study on BDS application (Dong et al., 2018), this study accounts for the deformation and enlargement of the nasal vestibule caused by the insertion of the nosepiece. This improvement enhances the anatomical accuracy of the model, leading to more realistic simulation of drug airflow and deposition patterns.

In this study, Fluent Meshing (ANSYS Inc., PA, USA) was used to prepare the computational mesh. To accurately capture the highly irregular shape of the nasal cavity, the flow domain was discretized using high-quality poly-hex core elements with a mesh size of 0.5 mm (Dong et al., 2022). A boundary layer of five layers of prisms with the first layer of polyhedral elements with a height of 0.02 mm was applied to the wall surface (Cai et al., 2023). The total number of mesh elements across all five models ranged from 2.1 million to 2.9 million. Examples of the surface mesh and interior slice mesh are shown in Fig. 3. As previously reported (Ma et al., 2024a), a characteristic line along the Y-axis, extending from the anterior section of the nasal cavity to the nasopharynx, was analyzed across three mesh resolutions: coarse (1,832,713 elements), medium (2,742,384 elements), and fine (3,404,041 elements) (Fig. 4). Increasing the mesh from 2.7 million to 3.4 million elements resulted in less than a 1 % change in average velocity and pressure, indicating mesh independence.

Due to the limited width in the vicinity of the nasal valve, poor nozzle-nasal valve alignment will filter most of the sprayed droplets and significantly reduce drug delivery performance (Patel, 2017). In this study, a generic bidirectional delivery system (BDS) was used. The rigid nosepiece geometry was obtained from CT imaging and model reconstruction, and subsequently inserted into all nasal models within the CAD environment. To achieve a snug fit, the nasal vestibule wall was slightly adjusted to accommodate the rigid nosepiece shape, ensuring a complete seal between the nosepiece and the nasal chamber. According to the plane of the nasal valve, the nosepiece tip was aimed at the center line of the nasal valve in order to optimize the insertion angle of the

Table 1
Demographic characteristics and surgical treatment.

ID	Sex	Age (y)	Left chamber			Right chamber		
			Surface area (mm^2)	Volume (mm^3)	SVR (mm^{-1})	Surface area (mm^2)	Volume (mm^3)	SVR (mm^{-1})
A	M.	30	16714.69	46877.20	0.36	12520.91	32837.60	0.38
B	M.	31	14127.43	45592.37	0.31	13335.87	41277.24	0.32
C	F.	58	15831.53	40802.90	0.39	13659.81	35079.92	0.39
D	M.	45	12096.29	36699.46	0.33	12487.14	40742.85	0.31
E	F.	57	16367.47	46111.93	0.35	15662.75	41393.43	0.38

M.: Male; F.: Female; SVR: surface area-to-volume ratio.

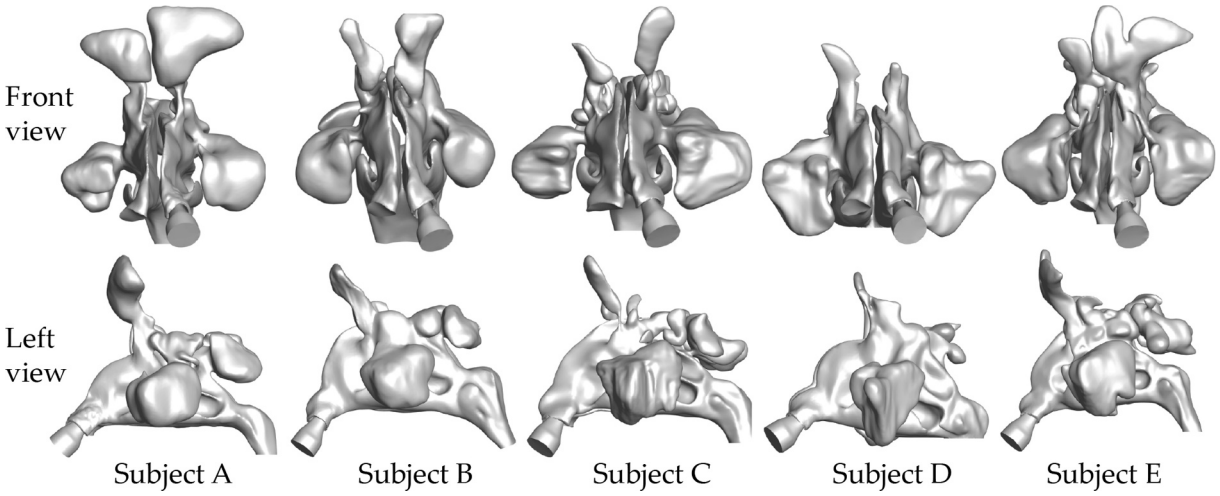

Fig. 1. Three-dimensional human nasal airway models of the five nasal subjects, each with the BDS nosepiece positioned in the left nasal vestibule.

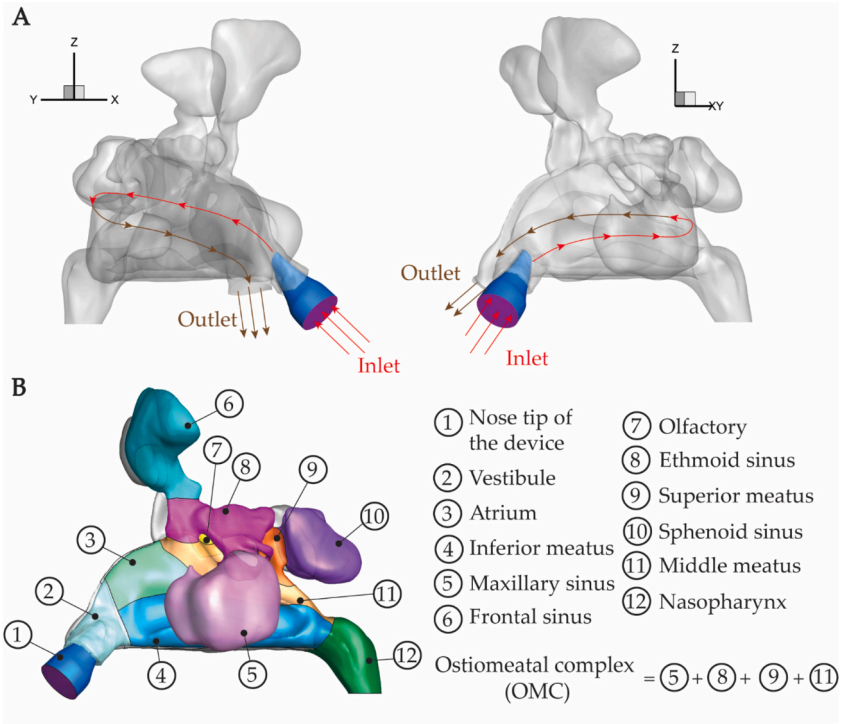

Fig. 2. Schematic diagram and surface partition of bidirectional drug delivery system (BDS) of a representative nasal airway model (i.e. model A). (A) Schematic diagram of airflow path; (B) Surface partition of left paranasal cavities.

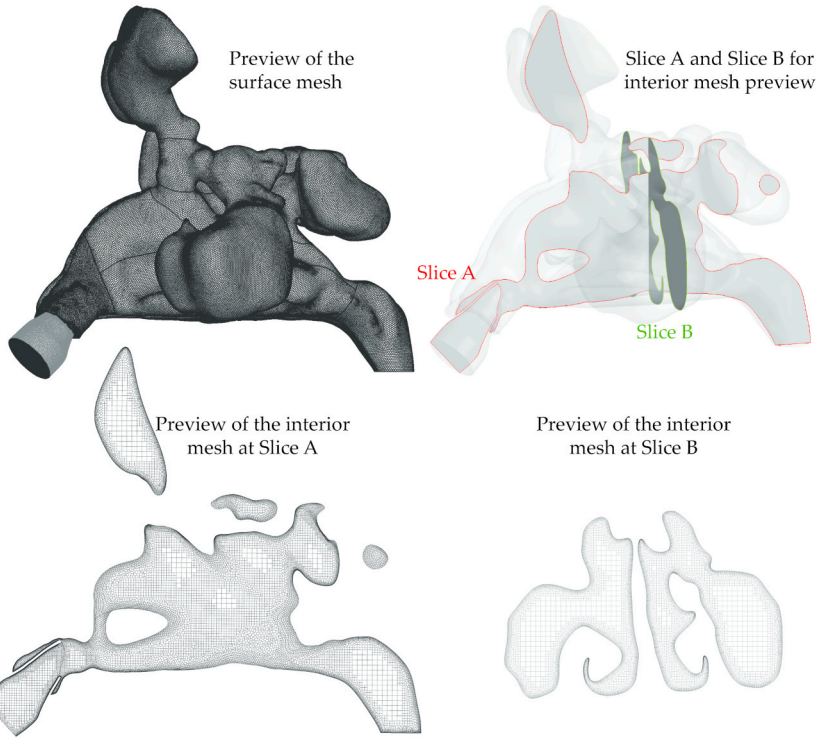

Fig. 3. Surface and interior slice mesh previews of a representative nasal airway model A, including the embedded bidirectional drug delivery nosepiece.

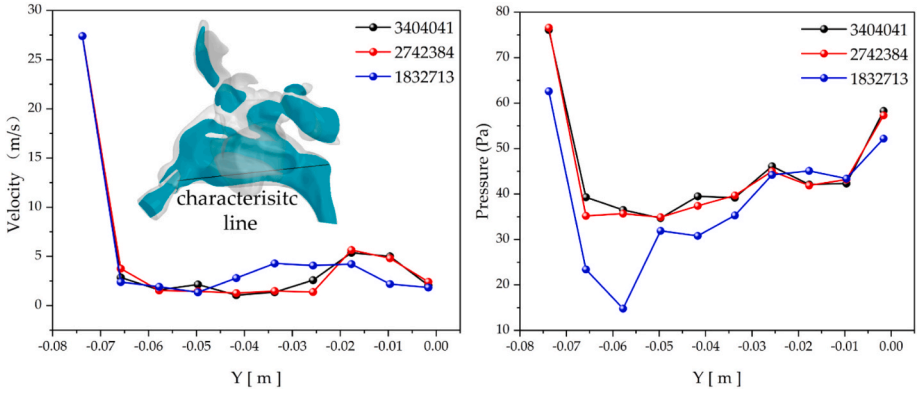

Fig. 4. Average velocity and pressure at a characteristic line along the *Y*-axis across three mesh resolutions in model E nasal cavity under exhalation flow rate of 30 L/min.

device nosepiece (Fig. 5A). Point A was defined as the centroid of the nasal valve plane. Points B, C, and D were positioned at half the maximum distance from point A in the superior, inferior, and lateral directions, respectively, serving as reference points to adjust and fine-tune the nosepiece orientation. We considered four representative nosepiece directions, namely the center direction (OA), upward tilt (OB), downward tilt (OC), and outward tilt (OD), and compared the effect of the insertion angle on the drug delivery performance. As the wall thickness of the nosepiece determines the effective particle release area, this study examined the impact of varying release areas by altering the nosepiece wall thickness (D = 0.5 mm, 1.0 mm, and 1.5 mm, respectively, Fig. 5B).

2.2. Airflow simulation and particle tracking

During exhalation, the soft palate is lifted, sealing off the nasopharyngeal airway. As a result, exhaled air carrying drug particles released from the nosepiece enters through the anterior of one nasal chamber, is diverted around the nasal concha, and exits through the opposite nostril. As shown in Table 2, three exhalation flow rates were considered: 15 L/min, 30 L/min, and 45 L/min. These values were selected to examine the effects of different driving flow rates on drug delivery performance. The inlet of the device nosepiece (the purple circular surface shown in Fig. 2A) is defined as the “velocity inlet”. The contralateral nostril is defined as the “pressure outlet”, and the velocity is calculated by dividing the specified flow rate by the inlet area. Although experimental work by Kelly et al. and numerical simulation conducted by Keyhani et al. suggested that airflow can be considered as laminar flow up to a rate of 24 L/min (Kelly et al., 2000; Keyhani et al., 1997), the insertion of the nosepiece is expected to induce significant flow acceleration and turbulence in the vestibular region of the left nasal cavity. Therefore, a low Reynolds number k-ω SST turbulence model is adopted, and the gravity direction is the negative Z-axis with a value of 9.8 m/s^2. Using ANSYS-Fluent v23.2, the flow field of the continuous gas phase under steady-state conditions was predicted by solving the full Navier-Stokes equations (Li et al., 2023; Kuprat et al., 2023). The QUICK scheme

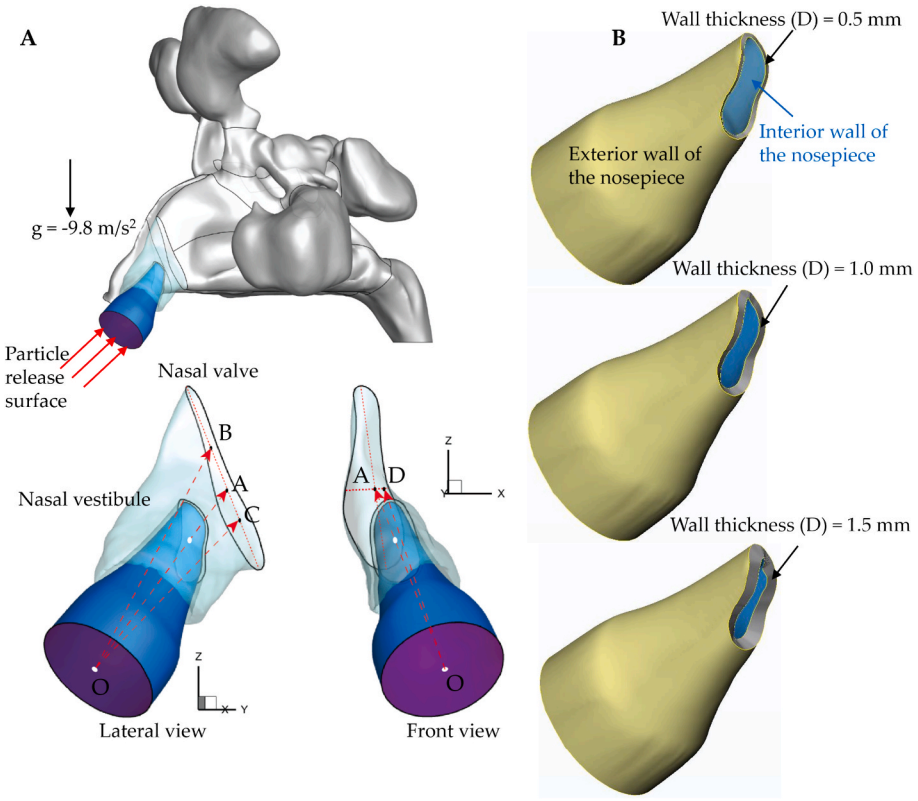

Fig. 5. Schematic diagram of insertion angle and wall thickness of device nosepiece. (A) Different orientation by varying insertion angle vertically (OA, OB, OC) and laterally (OD); (B) Different wall thickness.

Table 2
Key Influential Factors Affecting the Bidirectional Drug Delivery System (BDS).

Key Factors	Configurations
Insertion angle	4 orientations (OA, OB, OC, OD)
Wall thickness (D)	3 designs (0.5 mm, 1.0 mm, 1.5 mm)
Exhalation flow rate	3 flow rates (15 L/min, 30 L/min, 45 L/min)
Particle diameter (μm)	9 sizes (4.5, 7.5, 11.0, 15.5, 21.5, 37.5, 52.5, 75.0, 105)

was used to approximate the momentum equations, and the SIMPLE algorithm was applied for pressure–velocity coupling (Shen et al., 2023).

The Discrete Phase Model (DPM) with Lagrangian particle tracking was used. Particles were considered 'trapped' upon contact with the airway surfaces, which were modeled as no-slip, stationary walls.

Table 3 presents the particle size distribution of the BDS containing mometasone furoate, as measured by a laser particle size analyzer (HELOS IA-019, Germany). To approximate the realistic particle distribution in bidirectional delivery, we calculated the number of particles at each size based on a total dose mass of 100 mg per actuation.

Table 3
Drug particle size distribution through BDS.

Diameter (μm)	Interval fraction (%)	Particle Mass (mg)	Particle Number *(n)*
0–4.50	0.02	0.02	419,052
4.50–7.50	0.62	0.62	2,805,975
7.50–11.0	1.88	1.88	2,696,844
11.0–15.5	3.91	3.91	2,004,738
15.5–21.5	6.94	6.94	1,333,276
21.5 – 37.5	20.99	20.99	756,997
37.5 – 52.5	18.28	18.28	241,198
52.5 – 75.0	22.05	22.05	99,793
75.0–105	17.77	17.77	29,309

In this study, drug particles are assumed to be spherical, with a density equivalent to that of water. Nine representative particle sizes (4.5 μm, 7.5 μm, 11.0 μm, 15.5 μm, 21.5 μm, 37.5 μm, 52.5 μm, 75.0 μm, and 105.0 μm) were uniformly released from the inlet of the nosepiece (the purple plane shown in Fig. 5A) to simulate the delivery of drug aerosols through the nosepiece and their transport into the nasal chamber by exhalation-driven airflow. To simplify the simulation, the process by which particles are dispersed into the flow and enter the nosepiece was not modeled. Consequently, the particle distribution at the nosepiece entrance is assumed to be uniform, representing fully enriched aerosols within the duct.

The following equations were applied to estimate the mass deposition at various nasal regions:

$$M_{\text{Regional}} = \sum_i E_i m_i \tag{1}$$

$$V_i = \frac{4}{3}\pi r_i^3 \tag{2}$$

$$m_{p,i} = V_i \rho \tag{3}$$

$$m_i = n_i m_{p,i} \tag{4}$$

here, r_i is the characteristic radius for the size interval, ρ is the density of the particle (assumed equal to water in this study), $m_{p,i}$ is the single particle mass, n_i is the number of particles within this size interval, m_i is mass per size interval, E_i is deposition efficiency for size interval $\boldsymbol{i}$ within the region of interest, which is defined as the local deposition particle number divided by the number of particles that successfully enter the nasal passage. It is important to note that the particle size distribution used in this work is specific to the tested BDS formulation and device. As such, it may not be generalizable to other formulations or bidirectional delivery products. Given the dilute nature of the particle flow (volume

fraction < 0.1 %), particle–particle interactions were neglected, and a one-way coupling between the airflow and particles was assumed. This study primarily focuses on identifying the initial deposition sites of inhaled drug aerosols. To maintain a controlled and well-defined study scope, post-deposition processes such as mucociliary clearance were not considered.

2.3. 3D printing nasal replicas in Vitro- experiments

As shown in Fig. 6A, a realistic sinonasal cavity model (nasal subject C) was constructed to simulate particle deposition during nasal drug delivery. The model was assembled from multiple components to replicate the anatomical complexity of the nasal airways and sinuses. In the numerical simulations, the nasal cavity was segmented according to the anatomical subdivisions shown in Fig. 2 to enable regional deposition analysis. However, in the in vitro experiments, a larger-piece assembly strategy was adopted. This approach was necessary to maintain airtightness of the model, which is critical for ensuring the accuracy of bi-directional delivery performance. To ensure an airtight seal and accurate particle deposition within the sinus regions, sealing strips were designed to connect individual parts using screws and Bostik blue butadiene gum. Additionally, due to the increased complexity of disassembling smaller segments and accurately extracting regional dosage from each part, the experimental setup focused on larger structural components (including the flexible nasal vestibule, the lateral nasal walls, the septum, and the paranasal sinuses) rather than fine anatomical segmentation.

The nasal replica model was fabricated using a 3D printer (Lianruita-600, Hangzhou Meiyicheng Design Co., Ltd., China) with white resin 8000 material, which has a surface hardness of 56 Pa and a printing resolution of 0.1 mm in the X–Y plane. Additionally, a flexible silicone mold was used for the nasal vestibule region to account for its deformation under nasal administration conditions, enabling a more realistic simulation of drug particle distribution.

As shown in Figs. 6B and 6C, the nasal airway assembly was mounted on a custom model holder, and the trigger device (DH-ROBOTICS, China) was connected to a high-power vacuum flow pump (KARCHER, Professional series). The insertion depth and orientation angle of the BDS device in the nasal vestibule were adjusted after confirming airtightness.

Drug delivery was performed using an exhalation pressure of 6 kPa (equivalent to a volumetric flow rate of 19 L/min) and a computer-controlled pressing force of 100 N. The drug particles were administered into the sinonasal cavities via the trigger device, with one actuation per test, delivering 100 mg of formulation.

Immediately following each delivery, the model was disassembled, and deposited drug residues were thoroughly eluted from each anatomical region using a diluent solution composed of glacial acetic acid, acetonitrile, and water in a 5:1000:1000 (v/v/v) ratio. The eluent was collected into a 100 mL volumetric flask. After 5 min of ultrafiltration, 5 mL of the filtrate was extracted and passed through a syringe filter (PTFE membrane, 0.45 μm pore size, 02036331-TYLQ-0014, Titan).

High-Performance Liquid Chromatography (HPLC; Alliance e2695 Separations Module, Waters) was used to quantify the deposition dose in each region. After each test, the nasal model was thoroughly cleaned and dried in a ventilated environment.

To calculate the total dose administered for the in vitro experimental test, the dosing device was weighed separately before and after each test using an analytical laboratory balance (XSE205DU, METTLER TOLEDO) with an accuracy of 0.001 mg. Drug recovery efficiency was total dose recovery in the whole nasal model divide by total dose administered × 100 %.

2.4. Statistical analysis

Owing to the small sample size, which did not permit robust statistical comparisons, the results are reported as mean of the five nasal cavities. Statistical analysis was performed using SPSS 21.0 and Spearman correlation analysis was used. $P < 0.05$ was considered statistically significant.

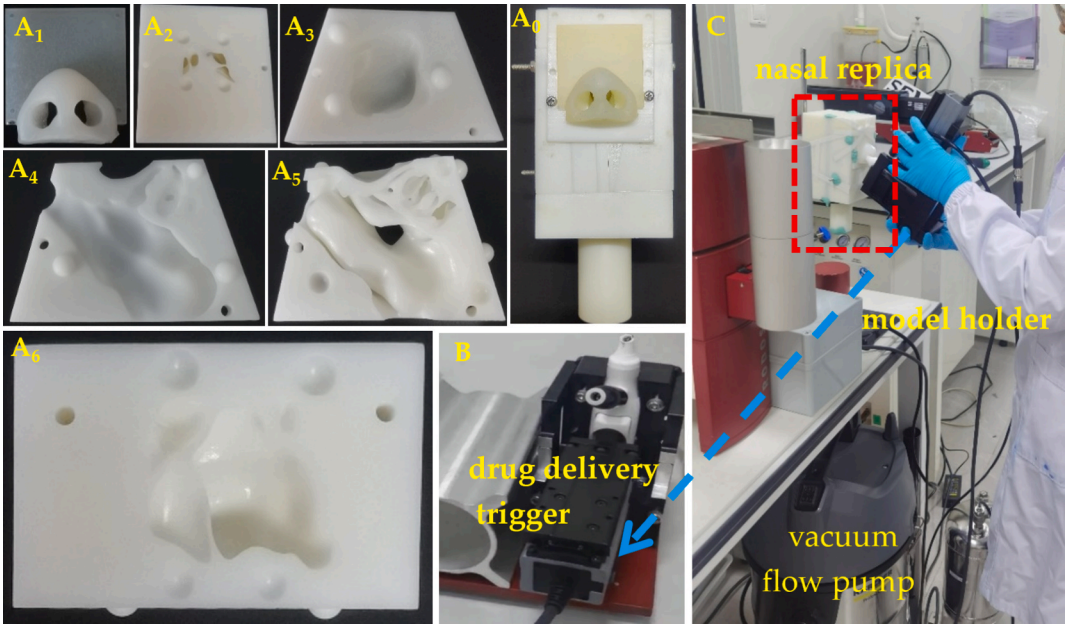

Fig. 6. In vitro experimental rig for measuring the drug aerosol delivery performance. ($A_{0\text{-}6}$): A_0 assembled 3D printed paranasal cavity model (nasal subject C), A_1 vestibule, A_2 bilateral frontal sinuses, A_3 maxillary sinus, A_4 septum, A_5 lateral of nasal cavity, A_6 sphenoid sinuses; (B) the drug delivery trigger of BDS; (C) bi-directional delivery system.

3. Results

3.1. Model validation

To validate the particle deposition model, a separate set of tests was conducted using an impaction parameter defined as $I = d_{ae}^2 Q$, where Q is the inhalation flow rate and d_{ae} is the aerodynamic diameter (Kuga et al., 2023). Monodispersed particles ranging from 1 to 30 μm in aerodynamic diameter were introduced into the sinonasal cavity model under exhalation flow rates of 15–45 L/min. The resulting deposition patterns were compared with relevant literature data to assess the accuracy of the simulation framework. This validation study was conducted independently of the case study scenario presented in this paper.

As shown in Fig. 7A, the deposition efficiency (DE) in the sinonasal cavities from our simulations exhibited an S-shaped curve, consistent with previously reported experimental data (Cheng et al., 2001; Kelly et al., 2004; Kelly et al., 2000) and numerical simulations (Hsu and Chuang, 2012; Siu et al., 2020b). The closest matching patterns were observed between our model and the results of Hsu and Chuang, while wider discrepancies were noted when compared with Siu et al., possibly due to differences in anatomical models (Hsu and Chuang, 2012; Siu et al., 2020b).

In addition to comparisons with peer studies, in vitro nasal administration was performed using a nasal replica of subject C (Fig. 6). The BDS-based drug delivery was conducted five times, and regional dosages in the vestibule, lateral wall (turbinates), and septum regions were quantified using HPLC. As previously mentioned, the equivalent driving airflow was 19 L/min. Numerical simulations for subject C were conducted using a polydisperse particle size distribution, as outlined in Table 3. The predicted regional dosages from the simulations were compared with the experimentally quantified values, as shown in Fig. 7B.

In general, the overall deposited dosage within the nasal cavity from the numerical simulation (90.62 mg) and the experimental measurement (82.19 ± 4.82 mg) showed close agreement, with a discrepancy of approximately 8.43 mg. There were approximately 44.54 ± 2.33 mg out of the 100 mg delivered per actuation reached the turbinates, and around 7.88 ± 3.72 mg was filtered out in the vestibule. In the simulated experiments, the nasal cavity exhibited a more pronounced disparity in deposition compared to the vestibular region, a phenomenon potentially attributable to the material properties of the models. To replicate the pliable and expandable characteristics of the human nasal vestibule, a flexible silicone was used as a biomimetic analogue (Fig. 7A). In contrast, the sinonasal cavities were 3D-printed using resin. Compared to the nasal vestibule, the resin surface is relatively smooth, resulting in a more pronounced liquid run-off effect.

Additionally, subtle variations were observed in the regional deposition patterns, particularly on the lateral and septal walls. The numerical simulation slightly underpredicted deposition on the lateral wall by 7.79 mg, while overestimating deposition on the septal wall by 16.23 mg compared to the experimental results. These differences can be attributed to several factors:

(i) In the experiment, the nozzle's outward-facing angle was not perfectly consistent with that used in the simulation, which likely increased deposition on the lateral wall while reducing it on the nasal septum.

(ii) Due to the anatomical structure of the middle and inferior turbinates, droplets deposited on the lateral wall are less influenced by gravity and tend to accumulate within the inferior meatus. In contrast, droplets deposited on the septal wall tend to coalesce and form a liquid film, which subsequently drains along the wall surface, leading to a further reduction in retained mass.

Consequently, an increase in deposited mass on the lateral wall and a corresponding reduction on the septal wall were observe in the experiment.

3.2. Airflow pattern

Airflow streamlines visualizing the exhalation pattern during BDS delivery are shown in Fig. 8, with the central OA direction indicating the insertion angle of the device. Nasal subject A was selected as the representative model. The exhaled air (with an exhalation rate of 15 L/min) enters the left nasal cavity through the device's inlet and accelerates due to the narrowing of the nasal valve. It then flows obliquely through the turbinate region at higher velocity, reaching the middle and upper parts of the nasal cavity, and impinges directly on the posterior wall of the ethmoidal sinus. As the cavity widens, airflow velocity gradually decreases. With the soft palate raised, the airflow continues into the nasopharynx and is redirected through the posterior nostril into the contralateral nasal cavity. Additionally, the streamlines show visible airflow extending into the sinus cavities, particularly the upper frontal sinuses and posterior sphenoid sinuses, where the ostium openings have been widened following FESS operation. This apparent sinus ventilation is attributed to the enlarged ostial openings in the post-surgical nasal geometry, which facilitates airflow entry into these regions.

3.3. Particle deposition patterns

In this study, the effects of four insertion angles, three device nosepiece wall thicknesses (0.5, 1.0 and 1.5 mm), and three exhalation flow rates (15, 30, and 45 L/min) on drug particle delivery by the BDS were investigated using the controlled variable method. Based on experimentally measured particle size distributions, the droplets mass delivered to the nasal cavity was calculated for each condition.

3.3.1. Particle deposition efficiency

1) Nosepiece Orientation

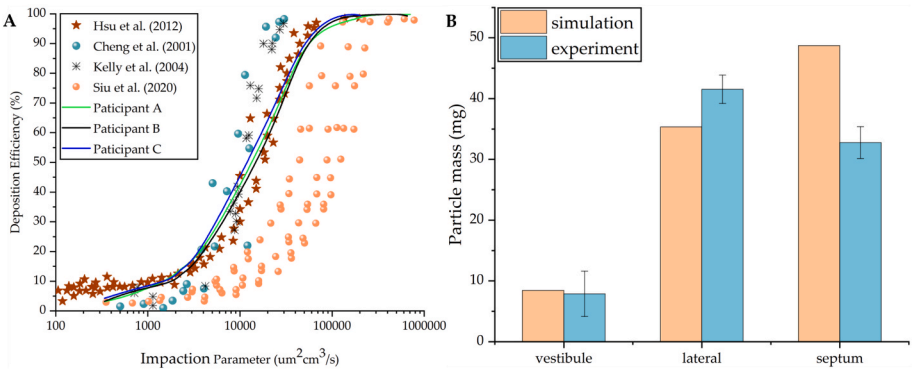

Fig. 7. Verification of drug particle deposition verification: (A) Comparison of deposition efficiency from this study with literature data; (B) Comparison of simulated deposition mass with in vitro experimental results.

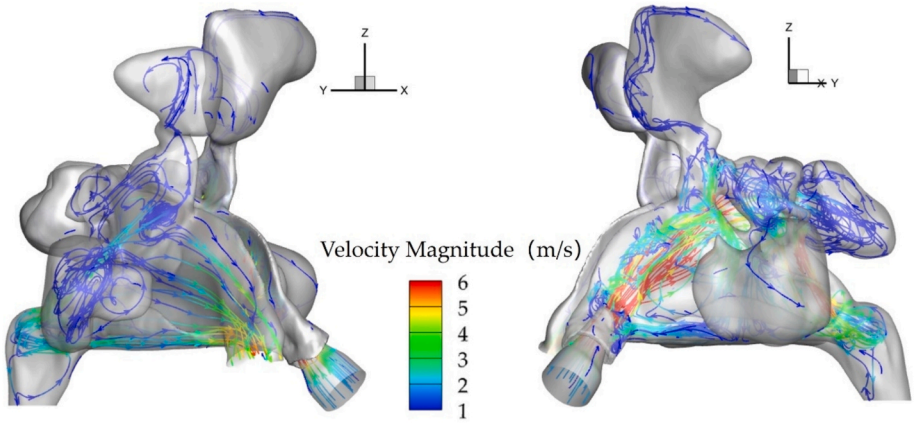

Fig. 8. Airflow streamlines during BDS delivery under 15 L/min exhalation flow rate and OA insertion angle, with a nosepiece wall thickness of D = 1.0 mm. Nasal subject A was selected as the representative model.

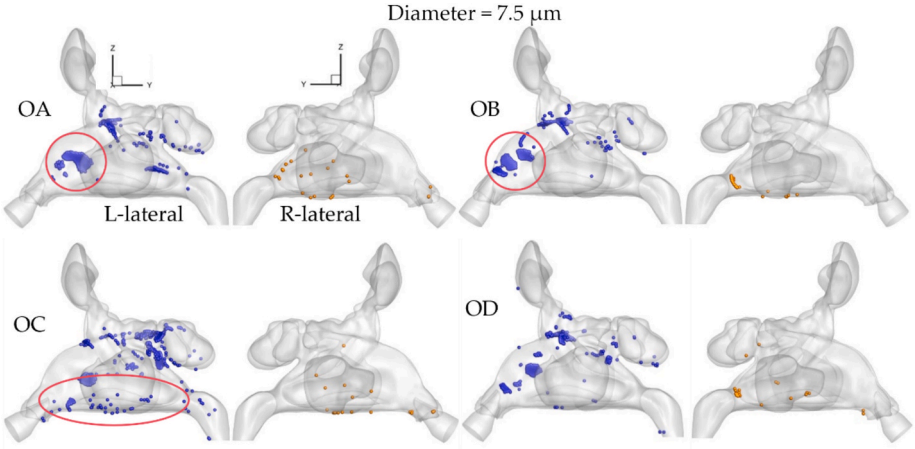

Fig. 9. Deposition distribution of BDS under 15 L/min exhalation flow rate and D was 1.0 mm. Different nosepiece orientation was achieved by varying insertion angle vertically (OA, OB, OC) and laterally (OD).

Fig. 9 presents the distribution of 7.5 μm particles in the sinonasal cavities delivered via BDS at four insertion angles, under an exhalation flow rate of 15 L/min and a nosepiece wall thickness of 1.0 mm. Blue dots represent deposition in the ipsilateral (administration side) nasal cavity, while orange dots indicate deposition in the contralateral cavity. The OC insertion angle resulted in increased deposition in the inferior meatus, whereas the OD angle produced a more uniform distribution across the ipsilateral nasal cavity compared to the centrally aligned OA angle. A portion of the residual drug aerosols that passed through the ipsilateral nasal cavity continued to travel into the contralateral cavity, with a small fraction ultimately escaping through the contralateral nostril. In the contralateral nasal cavity, particles primarily accumulated in the middle and lower regions, while deposition in the upper region was minimal.

Fig. 10 presents the DE profiles for the entire nasal cavity, the nasal septum, and the OMC across four insertion angles under exhalation flow rate of 15 L/min. As particle size increased, inertial impaction caused more particles to deposit in the anterior nasal septum. The results show that for particle diameters smaller than 15.5 μm, insertion angle had a noticeable impact on total nasal cavity DE. Specifically, the OB orientation (tilted upward) produced the highest total DE, followed by OA and OC (tilted downward). When the particle size was $\geq$ 15.5 μm, orientation had minimal influence on overall DE.

To evaluate delivery effectiveness to specific nasal regions, local DEs for the nasal septum and the OMC were further analyzed. Septal deposition was significantly higher for OA, OB, and OC orientations (all representing vertical tilting), while the OD orientation (lateral adjustment) consistently resulted in the lowest septal deposition across all particle sizes, approximately 20 % lower on average. Since septum deposition is typically associated with non-targeted, ineffective delivery, these results indicate that OD orientation is more favorable for efficient drug targeting.

This finding is reinforced by the OMC DE profile, where the OD orientation outperformed all other angles across the full range of particle sizes. Notably, OD achieved the highest OMC DE at a particle diameter of 11.0 μm, reaching a peak efficiency of 28.4 %. Across all five studied models, the OMC deposition efficiency was 28.4 % $\pm$ 12.14 % at this size particle. Given the clinical relevance of the OMC as a common site of sinus inflammation, the lateral OD orientation provides a more effective targeting strategy than vertical adjustments.

2) Nosepiece Wall Thicknesses.

Fig. 11 illustrates the drug particle deposition patterns in the sinonasal cavities for three different nosepiece wall thicknesses under a constant exhalation flow rate of 15 L/min. Increasing the wall thickness reduces the effective release area, which in turn increases the initial release velocity. As a result, thicker walls promote earlier deposition in the anterior region of the nasal cavity, primarily around the anterior portions of the turbinates, due to stronger inertial impaction. This change in deposition behavior leads to reduced particle transport to the posterior regions of the administering side, particularly the sphenoid sinus and nasopharynx, as indicated by red circles. A similar reduction is observed in the posterior region of the contralateral nasal cavity,

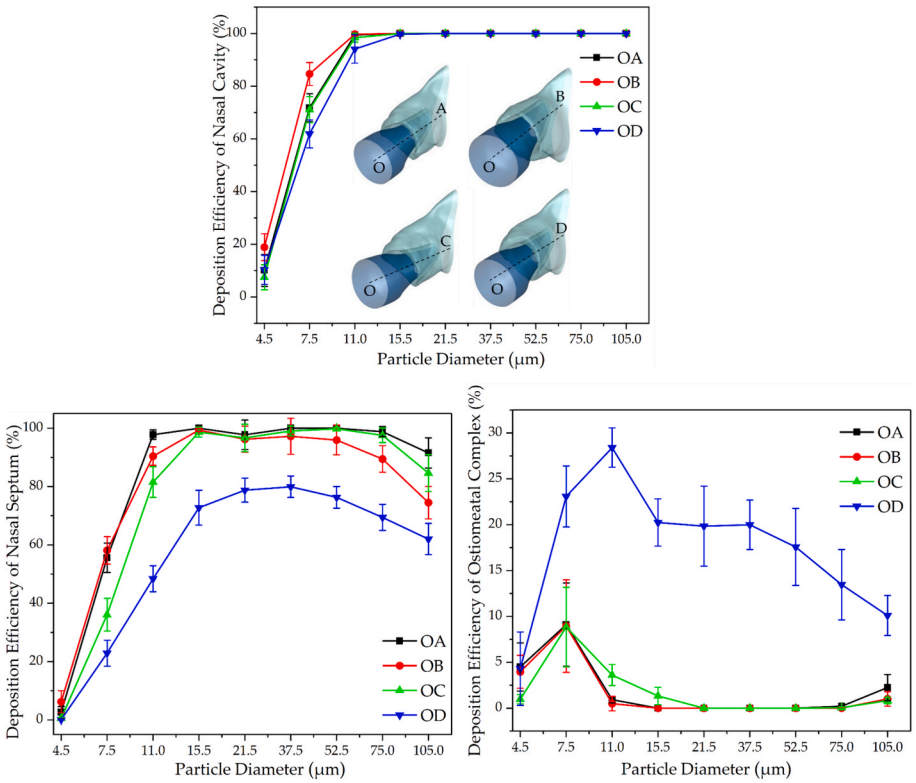

Fig. 10. Deposition efficiency under 15 L/min at different insertion angles of the device nosepiece. Nosepiece orientation was varied vertically (OA, OB, OC) and laterally (OD) to evaluate the impact on drug deposition within the nasal cavity.

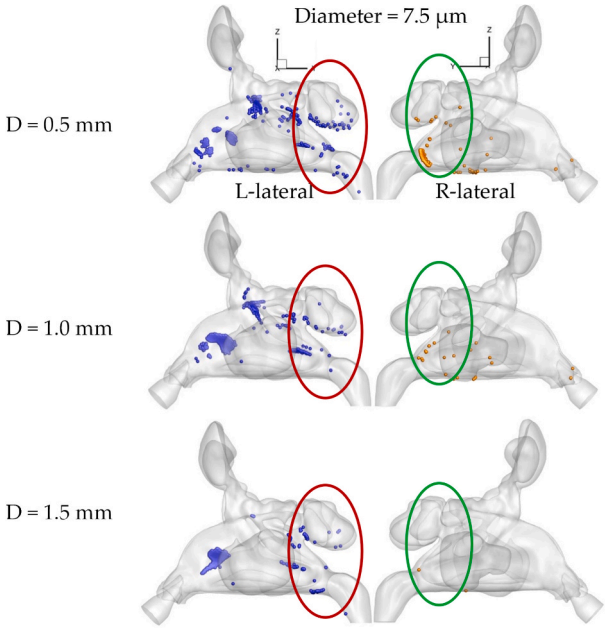

Fig. 11. Deposition distribution of BDS under 15 L/min exhalation flow rate with OA insertion angle.

highlighted by green circles. Overall, greater wall thickness limits particle penetration and decreases drug delivery efficiency to deeper and contralateral targets.

Fig. 12 presents the DE profiles for the entire nasal cavity, the nasal septum, and the OMC region at different wall thicknesses using the central orientation (OA) and exhalation flow rate of 15 L/min. For particle sizes below 15.5 μm, both overall nasal cavity and septum DEs increased with increasing wall thickness, indicating a positive relationship. For particle sizes equal to or greater than 15.5 μm, the DE values for the entire nasal cavity remained consistently at 100 % across all wall thicknesses.

Focusing on the OMC, the wall thickness of 0.5 mm consistently resulted in higher DE within the 7.5 to 15.5 μm particle size range. The highest OMC deposition was observed at a particle size of 11.0 μm, where the average DE reached 14.92 %. These results align with the spatial deposition patterns shown in Fig. 11 and provide quantitative confirmation of the influence of wall thickness on regional delivery efficiency.

Lastly, although minor increases (less than 4 %) in OMC DE were observed for particle sizes larger than 52.5 μm across all wall thicknesses, these increases may still contribute a substantial dosage to the targeted OMC region, as particle mass scales cubically with droplet size.

3) Exhalation Flow Rates.

Fig. 13 presents the DE profiles for the entire nasal cavity, nasal septum, and OMC region at three exhalation flow rates using the central orientation (OA). For particles smaller than 11.0 μm, both overall and septum DEs increased with flow rate, with 15 L/min showing the lowest values and 45 L/min the highest. For particle sizes greater than 11.0 μm, the overall DE remained largely unchanged across flow rates, while septum DE slightly decreased at sizes above 52.5 μm. At this size range, the septum DE at 45 L/min dropped from nearly 100 % to approximately 70 %, indicating increased particle transport toward other regions, including the OMC.

For OMC deposition, particles around 4.5 μm exhibited the highest DE values at 45 L/min and 30 L/min, both peaking near 15 %. As particle size increased to 15.5 μm, OMC DE decreased sharply, reaching nearly 0 %, then gradually increased for particle sizes above 52.5 μm. However, the increase remained minimal, with DE values below 3 %. At 15 L/min, the peak OMC DE occurred at 7.5 μm with an averaged value of 9.1 %.

The observed reduction in deposition on the septum wall and the

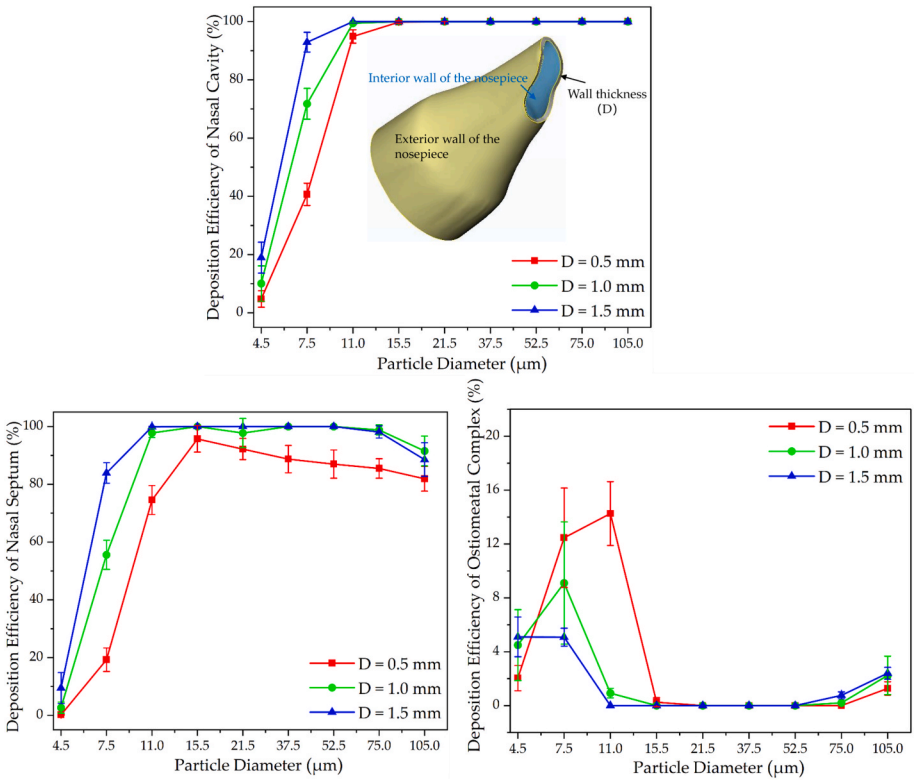

Fig. 12. Impact of nosepiece wall thickness on deposition efficiency in the nasal cavity, including overall DE, septum DE, and OMC DE across different particle sizes.

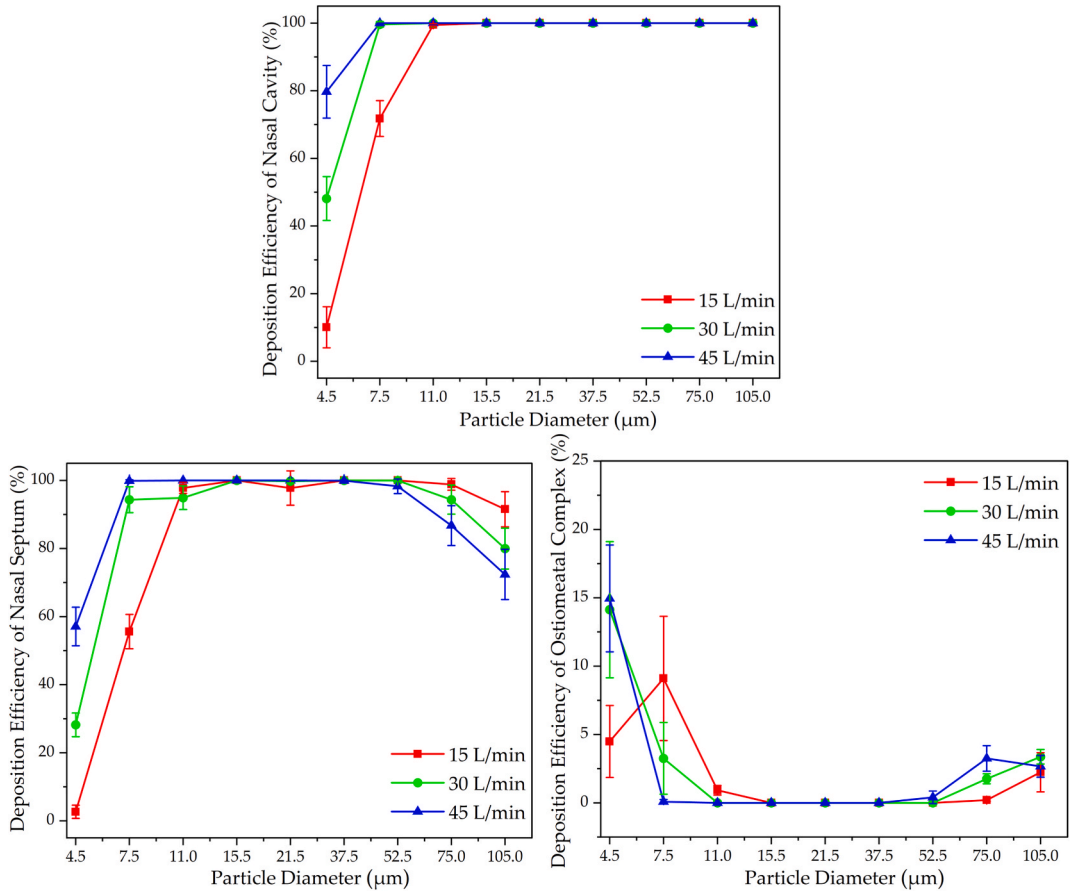

Fig. 13. Deposition efficiency in the nasal cavity, including overall DE, septum DE, and OMC DE at different exhalation flow rates using the central nosepiece orientation (OA).

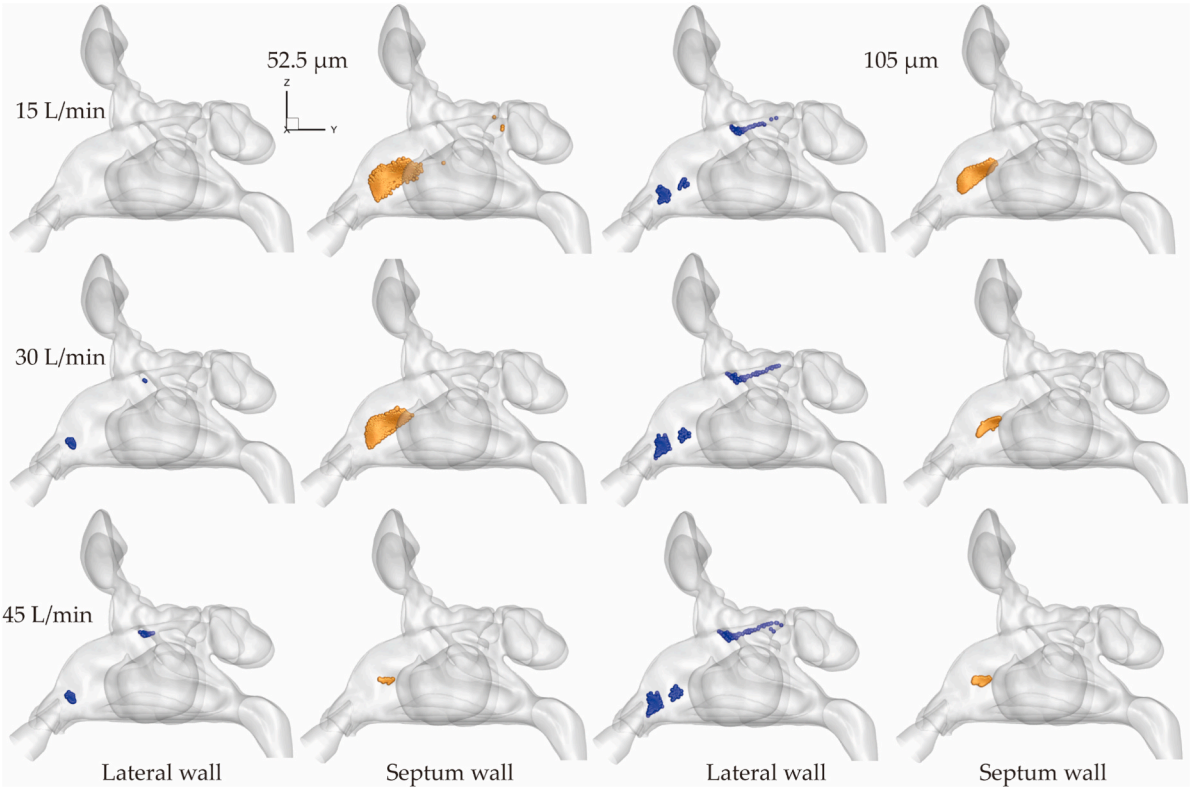

Fig. 14. Spatial deposition patterns in the nasal cavity model A under different exhalation flow rates using the central nosepiece orientation (OA). (Orange dots indicate deposition on the septum, while blue dots represent deposition on the opposite lateral wall).

slight increase in deposition on the lateral wall of the OMC region with increasing particle size and exhalation flow rate essentially represent a redistribution or shift of the delivered dosage, as illustrated in Fig. 14. The orange dots indicate deposition on the septum, while blue dots represent deposition on the opposite lateral wall. In general, a higher exhalation flow rate enables the released droplet clusters to reach the lateral wall more effectively, thereby reducing the number of particles deposited on the opposite septum wall. As the exhalation flow rate increases, the deposition of 52.5 μm and 105 μm particles on the lateral wall of the nasal cavity gradually increases, while their deposition on the nasal septum decreases. Moreover, compared with the 52.5 μm particles, the distribution of larger particles is more pronounced on both surfaces.

As observed in Figs. 12C and 13C of this study, a non-monotonic relationship between particle size and OMC deposition efficiency was identified under specific conditions. Therefore, in the correlation analysis of factors influencing OMC deposition, the relationship with particle size was not included. Fig. 15 presents the Spearman's rank correlation coefficients (ρ) between OMC deposition efficiency and three key parameters: insertion angle, nosepiece wall thickness, exhalation flow rate. Among these variables, insertion angle showed a statistically significant positive correlation with OMC deposition ($\rho = 0.679$, $p < 0.01$), indicating a strong association. Exhalation flow rate and wall thickness exhibited weak negative correlations ($\rho = -0.149$ and $\rho = -0.054$, respectively), though neither was statistically significant ($p > 0.05$). These results suggest that insertion angle plays a dominant role in influencing drug delivery to the OMC region, while the effects of flow rate, wall thickness, and particle size are relatively limited.

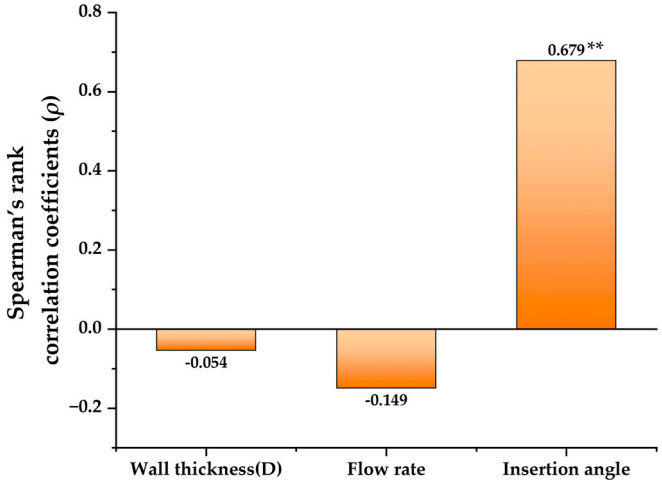

Fig. 15. Correlation analysis of deposition in the OMC and the influencing factors. (** indicates $p < 0.01$, positive values indicate positive correlation and negative values indicate negative correlation).

3.3.2. Mass distribution

Fig. 16 presents the mass distribution of deposited drug in the target OMC region across particle sizes under varying operational parameters, based on the measured polydisperse aerosol formulation with a total administered dose of 100 mg (see Table 3). The three subfigures illustrate the effect of (A) insertion angle, (B) nosepiece wall thickness, and (C) exhalation flow rate on the total deposited droplets mass in the nasal cavity. The results reveal that insertion angle had a substantial influence on OMC dosage. Specifically, the lateral OD orientation resulted in the highest OMC deposition, delivering approximately 15.02 ± 3.21 mg per actuation. In contrast, the vertical tilting angles (OA, OB, and OC) led to significantly lower deposition in the OMC, with dosage values below 0.7 mg. Particularly in the upward OB orientation resulted in the lowest OMC deposition, delivering approximately 0.10 ± 0.06 mg per actuation.

Nosepiece wall thickness also affected both the magnitude and the

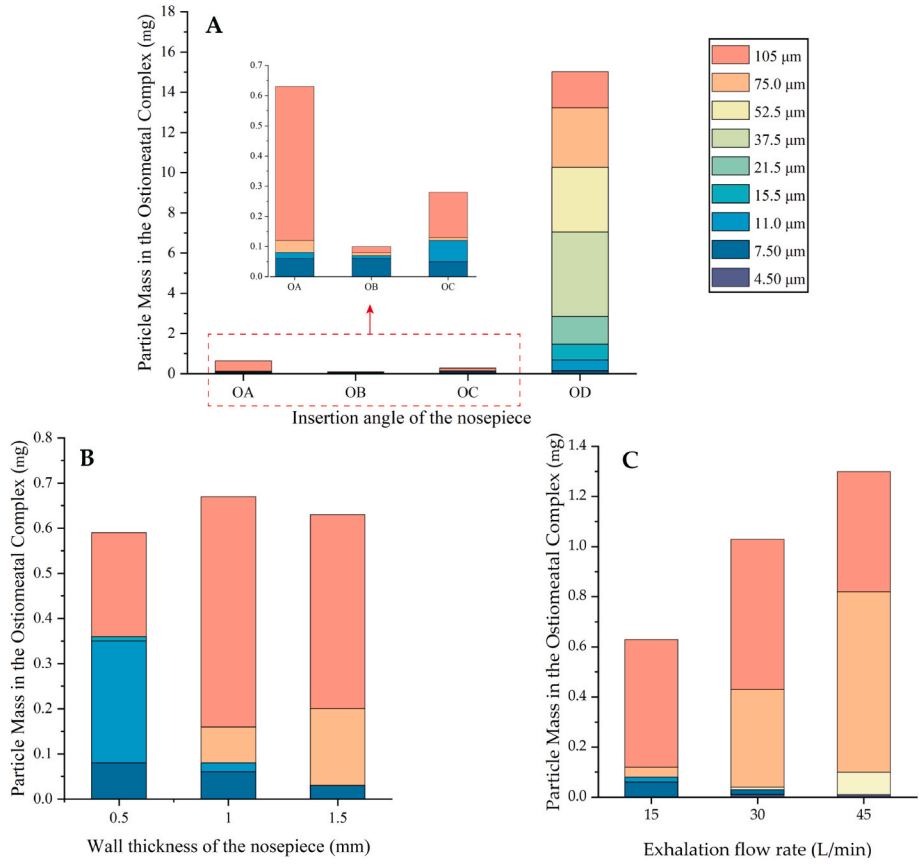

Fig. 16. Administered nasal mass distribution in the target OMC (ostiomeatal complex) region under different device conditions. (A) Effect of insertion angle (OA, OB, OC, OD) at a fixed exhalation flow rate of 15 L/min and nosepiece wall thickness of 1.0 mm. (B) Effect of nosepiece wall thickness (0.5 mm, 1.0 mm, 1.5 mm) at a fixed exhalation flow rate of 15 L/min and OA orientation. (C) Effect of exhalation flow rate (15, 30, and 45 L/min) at OA orientation and wall thickness of 1.0 mm.

particle size range of effective OMC deposition. As the wall became thicker, the contribution of smaller particles diminished, while that of larger particles became more pronounced. At a thickness of 0.5 mm, a distinct bimodal deposition pattern emerged, characterized by effective particle modes below 15.5 μm and above 75.5 μm. This configuration yielded a total deposited mass of approximately 0.6 mg in the OMC. As the wall thickness increased, deposition became increasingly limited to larger particles (primarily 75–105 μm).

The effect of exhalation flow rate (15, 30, and 45 L/min) at OA orientation and wall thickness of 1.0 mm was shown in Fig. 16C. Regarding exhalation flow rate, higher flow rates enhanced drug delivery to the OMC. At 45 L/min, the OMC deposition dosage increased to 1.3 mg, although the effective particle size range narrowed to approximately 52.5–105 μm. It would be valuable to further clarify how increasing the release velocity—whether by raising the flow rate or by changing cross-sectional area (wall thickness)—differently affects the deposition pattern. For instance, in this study, the deposited drug dose in the OMC region reached 1.3 mg at a high flow rate (45 L/min) with an optimal wall thickness (D = 1.0 mm), which is markedly higher than the 0.65 mg observed at a low flow rate (15 L/min) under the same wall thickness condition—effectively doubling the delivery efficiency.

4. Discussion

Based on the particle size distribution of the real BDS, this study employed CFD numerical simulations combined with in vitro experiments using 3D-printed sinonasal cavity models. For the first time, we systematically investigated the influence of nasal drug delivery device parameters on particle deposition within the nasal passages. This work examined the effects of device insertion angle, wall thickness, exhalation flow rate, and particle size on drug particle deposition patterns, and further quantified the mass distribution associated with actual BDS administration under varying operational conditions. The findings offer a systematically evaluation for better understanding drug delivery dynamics with BDS and support the optimized design of nasal delivery devices.

Although BDS can provide non-invasive and rapid treatment without first-pass effects, poorly designed nosepiece or incorrect use of BDS devices will significantly affect treatment outcomes (Rigaut et al., 2022). As with traditional nasal sprays, specific insertion angles of device are particularly important to reduce drug deposition in the anterior part of the nasal cavity (Bass et al., 2022). Tong et al. have studied the ideal insertion angle of traditional nasal sprays, and the results showed that the spray efficiency of OA in the central direction was better than that in the upper and lower directions (OB and OC) (Tong et al., 2016). They specifically pointed out that the optimal spray direction may vary between different matches of nasal sprayers and the nasal cavity, due to the interaction between the nasal sprayer and human nasal cavity dominating the drug delivery process. In this study, we examined the central insertion direction (OA) along with the upward (OB) and downward (OC) orientations. To reduce the direct impaction of larger particles on the nasal septum, a lateral orientation (OD) was also considered. Simulation results of the nosepiece–vestibule interaction indicated that the OD insertion angle provided more effective drug delivery compared to the other three orientations. When the nosepiece axis is aligned to directly target the OMC, larger droplets are more likely to deposit in this region. This approach is termed the “Line of Sight” (LoS) protocol by Basu et al. (2020). The CFD-guided LoS protocol was shown to significantly enhance topical drug delivery to targeted sinonasal sites compared to conventional administration techniques (Basu et al., 2020).

However, direct identification of the OMC region remains challenging in clinical practice. To facilitate identification of the optimal delivery angle, this study uses the nasal valve as an external anatomical landmark to guide and achieve correct OD orientation.

As is well understood, when the outer contour of the nosepiece remains constant, increasing wall thickness reduces the effective cross-sectional area at the outlet. This change alters the initial velocity of released drug particles. Within the examined wall thickness range of 0.5–1.5 mm, thicker walls resulted in higher initial particle velocities and kinetic energies, leading to greater overall deposition and mass distribution in the nasal cavity under a constant exhalation flow rate. However, the local particle deposition and mass distribution of OMC were different. The current study found that for smaller particles ($\leq$ 15.5 μm), the local DE in the OMC was highest at a wall thickness of 0.5 mm, with 11.0 μm particles achieving peak DE at an average of 14.92 %. In contrast, larger particles ($\geq$ 52.5 μm) showed higher local DE at wall thicknesses of 1.0 mm and 1.5 mm. These trends were consistent with the corresponding local mass distribution profiles observed in the OMC region.

In addition, changes in exhalation flow can alter expiratory dynamic delivery performance to some extent (Yarragudi et al., 2020). Higher exhalation flow increases the efficiency of intranasal aerosol deposition, with less outflow from the contralateral nostril. Due to the airflow direction at the nasopharynx, the administration side adjacent to the device (the left side in this study) receives aerosols preferentially, and the rate of intranasal deposition is much higher than that of the right side. Meanwhile, the deposition of particles in the left nasal cavity was relatively concentrated, and there was obvious particle aggregation in the nasal septum and middle meatus. Hu et al. found a similar phenomenon when comparing the effects of BDS with transnasal nebulization in children upper airway (Hu et al., 2024). We focused on the administration effect in OMC and found that there are no noticeable changes of the DE in OMC, with the increase of exhalation flow rate. While the spray mass distribution gradually increased, which was related to the relatively large volume of large particles.

Finally, among all variables analyzed, insertion angle emerged as the most influential factor, showing a strong positive correlation with OMC deposition efficiency and resulting in the highest mass dosage when oriented laterally (OD). In contrast, wall thickness and exhalation flow rate had only modest or condition-specific effects, primarily by modulating particle velocity and narrowing the effective particle size band. These findings underscore the importance of optimizing device orientation and structural design to enhance site-specific drug delivery, especially when targeting challenging anatomical regions such as the OMC. This work provides a methodological foundation and practical direction for improving nasal drug delivery strategies and device development, with potential implications for treating refractory sinonasal conditions more effectively.

In this study, we focused on the BDS scenario, where drug-laden droplets were considered as the delivered phase. The process is primarily driven by a steady exhalation airflow rather than an inhalation flow pattern (Kuprat et al., 2023). We acknowledge that transient flow effects, particularly during the initial phase of exhalation, may influence droplet transport and deposition, thereby contributing to variations in overall delivery performance.

Additionally, droplet size may vary in humid environments as a result of heat and mass exchange caused by the hygroscopic effect. However, since the nasal cavity constitutes a relatively short transport pathway compared with pulmonary delivery (Chalvatzaki et al., 2018), hygroscopic growth and evaporation are expected to have only a minor impact on deposition outcomes within the nasal region.

Moreover, the primary objective of this study was to evaluate the influence of device-related operational factors (including nosepiece insertion angle, wall thickness, and exhalation flow rate) on BDS performance. Simplifications including steady-state flow and non-evaporating droplets were adopted to isolate these effects and ensure computational feasibility.

This study primarily focused on identifying the initial deposition sites of inhaled drug aerosols. To allow for a targeted investigation scope, the nasal cavity was modeled as a rigid structure, and post-deposition processes such as mucociliary clearance, particle shift and dissolution, and interactions with mucus, cilia, and vascular structures were not considered. Future studies could incorporate more physiological features to provide a more comprehensive understanding of airflow behavior and particle transport within the sinonasal cavities under various respiratory conditions.

5. Conclusion

In this study, we developed a comprehensive approach to better understand the mechanism of bidirectional nasal delivery and evaluated the influencing factors of the delivery performance of BDS for the first time based on true particle size distribution and realistic human nasal subjects. Simulation results were compared with in vitro model experiments in laboratory settings. The results confirm that aerosol delivery to the targeted OMC region is more effectively achieved by adjusting the nosepiece laterally outward. Compared with the insertion angle, the device wall thickness and exhalation flow rate had a moderate effect on the mass distribution in the OMC. Moreover, the current study indicates a positive correlation between exhalation flow rate and targeted OMC mass deposition within the 15–45 L/min range for particles $\leq$ 15.5 μm and $\geq$ 52.5 μm. Our research lays the groundwork for innovative strategies to optimize drug delivery and improve treatment outcomes for CRSwNP following FESS.

CRediT authorship contribution statement

Ruiping Ma: Writing – original draft, Validation, Methodology, Formal analysis, Conceptualization. **Siping Sun:** Resources. **Yusheng Wang:** Validation. **Feilun Yang:** Investigation. **Zehui Li:** Validation. **Botao Wang:** Resources. **Jingguo Chen:** Funding acquisition. **Bin Sun:** Conceptualization. **Guoxi Zheng:** Methodology, Funding acquisition, Conceptualization. **Shaokoon Cheng:** Writing – review & editing. **Ya Zhang:** Validation, Methodology, Funding acquisition, Conceptualization. **Jingliang Dong:** Writing – review & editing, Validation, Supervision, Methodology, Funding acquisition.

Declaration of competing interest

The authors declare that they have no known competing financial interests or personal relationships that could have appeared to influence the work reported in this paper.

Acknowledgements

The financial supports provided by the Key Research and Development Program of Shaanxi Province (2024SF-YBXM-345, 2025JC-YBQN-1075, and 2025JC-YBQN-1038), and the Australian Research Council [grant number DE210101549] are gratefully acknowledged.

Data availability

Data will be made available on request.

References

Bass, K., Momin, M.A.M., Howe, C., Aladwani, G., Strickler, S., Kolanjiyil, A.V., Hindle, M., DiBlasi, R.M., Longest, W., 2022. Characterizing the effects of nasal prong interfaces on aerosol deposition in a preterm infant nasal model. AAPS PharmSciTech 23.

Basu, S., Holbrook, L.T., Kudlaty, K., Fasanmade, O., Wu, J., Burke, A., Langworthy, B. W., Farzal, Z., Mamdani, M., Bennett, W.D., Fine, J.P., Senior, B.A., Zanation, A.M., Ebert Jr., C.S., Kimple, A.J., Thorp, B.D., Frank-Ito, D.O., Garcia, G.J.M., Kimbell, J.

S., 2020. Numerical evaluation of spray position for improved nasal drug delivery. Sci. Rep. 10, 10568.
Cai, X.Y., Dong, J.L., Milton-McGurk, L., Lee, A., Shen, Z.W., Chan, H.K., Kourmatzis, A., Cheng, S.K., 2023. Understanding the effects of inhaler resistance on particle deposition behaviour - a computational modelling study. Comput. Biol. Med. 167.
Calmet, H., Inthavong, K., Eguzkitza, B., Lehmkuhl, O., Houzeaux, G., Vázquez, M., 2019. Nasal sprayed particle deposition in a human nasal cavity under different inhalation conditions. PLoS One 14.
Cassano, R., Servidio, C., Trombino, S., 2021. Biomaterials for drugs nose-brain transport: a new therapeutic approach for neurological diseases. Materials 14.
Chalvatzaki, E., Lazaridis, M., 2018. A dosimetry model of hygroscopic particle growth in the human respiratory tract. Air Qual. Atmos. Health 11, 471–482.
Cheng, Y.S., Fu, C.S., Yazzie, D., Zhou, Y., 2001. Respiratory deposition patterns of salbutamol pMDI with CFC and HFA-134a formulations in a human airway replica. Journal of Aerosol Medicine-Deposition Clearance and Effects in the Lung 14, 255–266.
Corcoran, T.E., 2015. Imaging in aerosol medicine. Respir. Care 60, 850–855.
Djupesland, P.G., 2013. Nasal drug delivery devices: characteristics and performance in a clinical perspective-a review. Drug Deliv. Transl. Res. 3, 42–62.
Djupesland, P.G., Messina, J.C., Palmer, J.N., 2020. Deposition of drugs in the nose and sinuses with an exhalation delivery system vs conventional nasal spray or high-volume irrigation in Draf II/III post-surgical anatomy. Rhinology 58, 175–183.
Djupesland, P.G., Skretting, A., 2012. Nasal deposition and clearance in man: comparison of a bidirectional powder device and a traditional liquid spray pump. J. Aerosol Med. Pulm. Drug Deliv. 25, 280–289.
Djupesland, P.G., Skretting, A., Winderen, M., Holand, T., 2004. Bi-directional nasal delivery of aerosols can prevent lung deposition. Journal of Aerosol Medicine-Deposition Clearance and Effects in the Lung 17, 249–259.
Djupesland, P.G., Skretting, A., Winderen, M., Holand, T., 2006. Breath actuated device improves delivery to target sites beyond the nasal valve. Laryngoscope 116, 466–472.
Dong, J.L., Shang, Y.D., Inthavong, K., Chan, H.K., Tu, J.Y., 2018. Numerical comparison of nasal aerosol administration systems for efficient nose-to-brain drug delivery. Pharm. Res. 35.
Dong, J.L., Sun, Q.Y., Shang, Y.D., Zhang, Y., Tian, L., Tu, J.Y., 2022. Numerical comparison of inspiratory airflow patterns in human nasal cavities with distinct age differences. International Journal for Numerical Methods in Biomedical Engineering 38.
Farnoud, A., Tofighian, H., Baumann, I., Martin, A.R., Rashidi, M.M., Menden, M.P., Schmid, O., 2021. Pulsatile bi-directional aerosol flow affects aerosol delivery to the intranasal olfactory region: a patient-specific computational study. Frontiers in Pharmacology 12.
Hosseini, S., Golshahi, L., 2019. An in vitro evaluation of importance of airway anatomy in sub-regional nasal and paranasal drug delivery with nebulizers using three different anatomical nasal airway replicas of 2-, 5-and 50-Year old human subjects. Int. J. Pharm. 563, 426–436.
Hsu, D.J., Chuang, M.H., 2012. In-vivo measurements of micrometer-sized particle deposition in the nasal cavities of Taiwanese adults. Aerosol Sci. Tech. 46, 631–638.
Hu, Z.Z., Cheng, S.K., Sun, S.P., Wang, Y.S., Lou, M., Ma, R.P., Gong, M.J., Yang, F.L., Zheng, G.X., Zhang, Y., Dong, J.L., 2024. Numerical and experimental evaluation of nasopharyngeal aerosol administration methods in children with adenoid hypertrophy. Int. J. Pharm. 653.
Kelly, J.T., Asgharian, B., Kimbell, J.S., Wong, B.A., 2004. Particle deposition in human nasal airway replicas manufactured by different methods. Part I: Inertial regime particles. Aerosol Sci. Tech. 38, 1063–1071.
Kelly, J.T., Prasad, A.K., Wexler, A.S., 2000. Detailed flow patterns in the nasal cavity. J. Appl. Physiol. 89, 323–337.
Keyhani, K., Scherer, P.W., Mozell, M.M., 1997. A numerical model of nasal odorant transport for the analysis of human olfaction. J. Theor. Biol. 186, 279–301.
Kuga, K., Kizuka, R., Khoa, N.D., Ito, K., 2023. Effect of transient breathing cycle on the deposition of micro and nanoparticles on respiratory walls. Computer Methods and Programs in Biomedicine 236.
Kuprat, A.P., Price, O., Asgharian, B., Singh, R.K., Colby, S., Yugulis, K., Corley, R.A., Darquenne, C., 2023. Automated bidirectional coupling of multiscale models of aerosol dosimetry: validation with subject-specific deposition data. Journal of Aerosol Scicence 174, 106233.
Li, J., Ma, J.W., Dong, J.L., Yang, W., Tu, J.Y., Tian, L., 2023. Total and regional microfiber transport characterization in a 15th-Generation human respiratory airway. Computers in Biology and Medicine 163.
Liu, Y.X., Wu, D.W., 2023. Bi-directional nasal drug delivery systems: a scoping review of nasal particle deposition patterns and clinical application. Laryngoscope Investigative Otolaryngology 8, 1484–1499.
Ma, R.P., Hu, Z.Z., Tian, L., Zheng, G.X., Wang, Y.S., Chen, X.L., Lou, M., Gong, M.J., Wang, B.T., Yang, F.L., Dong, J.L., Zhang, Y., 2024a. Numerical and experimental analysis of pollen inhalation exposure in nasal airways following various middle turbinectomy. Science of the Total Environment 907.
Ma, R.P., Tian, L., Wang, Y.S., Sun, S.P., Zhang, J.B., Lou, M., Hu, Z.Z., Gong, M.J., Yang, F.L., Zheng, G.X., Dong, J.L., Zhang, Y., 2024b. Comparative investigation of transport and deposition of nebulized particles in nasal airways following various middle turbinectomy. Rhinology 62, 223–235.
Patel, R.G., 2017. Nasal anatomy and function. Facial Plast. Surg. 33, 3–8.
Rigaut, C., Deruyver, L., Goole, J., Haut, B., Lambert, P., 2022. Instillation of a dry powder in nasal casts: parameters influencing the olfactory deposition with uni- and bi-directional devices. Frontiers in Medical Technology 4.
Shen, Z.W., Dong, J.L., Milton-McGurk, L., Cai, X.Y., Gholizadeh, H., Chan, H.K., Lee, A., Kourmatzis, A., Cheng, S.K., 2023. Numerical analysis of airflow and particle deposition in multi-fidelity designs of nasal replicas following nasal administration. Computer Methods and Programs in Biomedicine 241.
Siu, J., Dong, J.L., Inthavong, K., Shang, Y.D., Douglas, R.G., 2020a. Quantification of airflow in the sinuses following functional endoscopic sinus surgery. Rhinology 58, 257–265.
Siu, J., Shrestha, K., Inthavong, K., Shang, Y.D., Douglas, R., 2020b. Particle deposition in the paranasal sinuses following endoscopic sinus surgery. Computers in Biology and Medicine 116.
Tong, X.W., Dong, J.L., Shang, Y.D., Inthavong, K., Tu, J.Y., 2016. Effects of nasal drug delivery device and its orientation on sprayed particle deposition in a realistic human nasal cavity. Comput. Biol. Med. 77, 40–48.
Wofford, M.R., Kimbell, J.S., Frank-Ito, D.O., Dhandha, V., McKinney, K.A., Fleischman, G.M., Ebert, C.S., Zanation, A.M., Senior, B.A., 2015. A computational study of functional endoscopic sinus surgery and maxillary sinus drug delivery. Rhinology 53, 41–48.
Xi, J.X., Wang, Z.X., Nevorski, D., White, T., Zhou, Y., 2017. Nasal and olfactory deposition with normal and bidirectional intranasal delivery techniques: in vitro tests and numerical simulations. J. Aerosol Med. Pulm. Drug Deliv. 30, 118–131.
Xi, J.X., Wang, Z.X., Si, X.A., Zhou, Y., 2018. Nasal dilation effects on olfactory deposition in unilateral and bi-directional deliveries: in vitro tests and numerical modeling. Eur. J. Pharm. Sci. 118, 113–123.
Yarragudi, S.B., Kumar, H., Jain, R., Tawhai, M., Rizwan, S., 2020. Olfactory targeting of microparticles through inhalation and bi-directional airflow: effect of particle size and nasal anatomy. J. Aerosol Med. Pulm. Drug Deliv. 33, 258–270.